

Mitigating spikes in fermion Monte Carlo methods by reshuffling measurements

Maksim Ulybyshev^{1,*} and Fakher Assaad^{1,†}

¹*Institute for Theoretical Physics, Julius-Maximilians-Universität Würzburg, 97074 Würzburg, Germany*

We propose a method to mitigate heavy-tailed distributions in fermion Quantum Monte Carlo simulations originating from zeros of the fermion determinant. We show that by merely changing the synchronization between local updates and computation of observables, one can reduce the prefactor of the heavy-tailed distribution, thus substantially suppressing statistical fluctuations of observables. The method is especially suitable for local observables similar to e.g. double occupancy, where the resulting speedup can reach two orders of magnitude. For observables, containing spatial correlators, the speedup is more moderate, but still ranges between five and ten. Our results are independent on the nature of the auxiliary field, discrete or continuous, and pave the way to improve measurement strategies for Hybrid Monte Carlo simulations.

PACS numbers: 11.15.Ha, 02.70.Ss, 71.10.Fd

Keywords: Hubbard model, Quantum Monte Carlo

I. INTRODUCTION

Many numerical and analytical schemes for identical fermions involve the fermion determinant. This quantity possesses zeros that are at the origin of many issues in Quantum Monte Carlo (QMC) methods [1–6]. This stems from the fact that although the weight of the configuration is proportional to the fermion determinant, the Green function – required to compute observables – corresponds to the inverse of the fermion matrix. Hence, if the stochastic walk is close to a zero of the fermion determinant, then observables will show spikes, Fig. 1, thus potentially leading to a fat tailed distribution [7]. Here we show that the tail of this distribution can be substantially reduced in magnitude, at zero cost, by merely reshuffling the sequence of measurements.

Our intuition is based on the following argument. The acceptance of local updates in fermion Monte Carlo is based on the local Green function. If this quantity is big, due to proximity of a zero mode, then the acceptance will be close to unity, and the Monte Carlo walk will move away from the zero mode. Hence if we measure local observables just after the update of the local site, we conjecture that this synchronization will mitigate spikes as opposed to measurement schemes where updates and the calculation of observables are not correlated.

We now state our conjecture more precisely. Fermion Monte Carlo methods rely on a path integral formulation of the partition function:

$$Z = \int D\{s_{i,\tau}\} e^{-S(\{s_{i,\tau}\})}. \quad (1)$$

Here, (i, τ) is a space-time index and the integration over the fields $s_{i,\tau}$ is carried out with Monte Carlo methods. We will not dwell on the negative sign problem and thereby assume that the action S is a real function

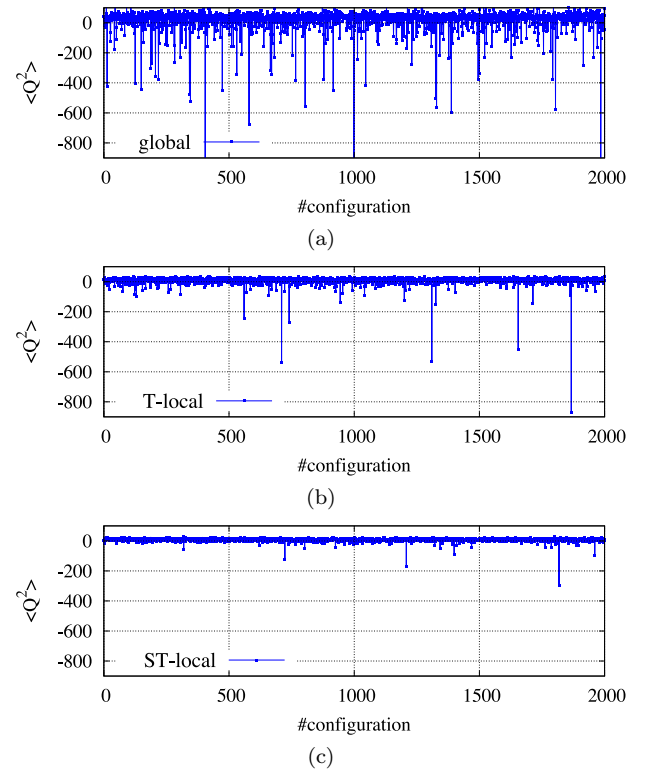


FIG. 1. Sublattice charge fluctuations of Eq. 33 for the global, Eq. 2 (upper plot), T-local, Eq. 3 (middle plot) and ST-local Eq. 4 (lower plot) schemes. Calculations were done on a $6 \times 6 \times 256$ hexagonal lattice at $U = 5.0$ and $\beta = 20.0$ using the SU(2) symmetrical discrete Hubbard Stratonovich (HS) field within a standard local update BSS-QMC algorithm [8].

of the fields. Let $C_{i,\tau}^n$ be the configuration obtained after updating the field at space-time site i, τ of the n^{th} sweep and $O_{i,\tau}(C)$ the value of a local variable for the configuration C . Note that a sweep corresponds to updating all fields in the space time lattice. We will consider three different ways of synchronizing local updates of the fields $s_{i,\tau}$ and measurement of observables.

* Maksim.Ulybyshev@physik.uni-wuerzburg.de

† Fakher.Assaad@physik.uni-wuerzburg.de

- Global scheme:

$$\langle O \rangle = \frac{1}{N} \sum_{n=1}^N \sum_{i,\tau} O_{i,\tau}(C_{V,L\tau}^n). \quad (2)$$

One carries out the measurement after having updated all the sites $i : 1 \cdots V$ and time slices $\tau : 1 \cdots L_\tau$. This measurement scheme is used in Langevin [8–10] or Hybrid Monte Carlo (HMC) calculations [3, 11, 12].

- Time(T)-local scheme (standard for present-day BSS-QMC algorithms [13]):

$$\langle O \rangle = \frac{1}{N} \sum_{n=1}^N \sum_{i,\tau} O_{i,\tau}(C_{V,\tau}^n). \quad (3)$$

One carries out the measurement of the observable $O_{i,\tau}$ at a given time slice τ after having updated all fields on this time slice $i : 1 \cdots V$.

- Space-Time(ST)-local scheme:

$$\langle O \rangle = \frac{1}{N} \sum_{n=1}^N \sum_{i,\tau} O_{i,\tau}(C_{i,\tau}^n). \quad (4)$$

In this case the measurement of local observables $O_{i,\tau}$ is carried out after each local update on the same site.

Our claim is that in the presence of zeros of the fermion determinant, the estimates 2, 3 and 4 perform substantially different in terms of the statistical error bars, despite yielding equivalent values for the averages of observables. Note that in each scheme, we carry out the same amount of measurements such that no additional computational cost is involved. We merely reshuffle the ordering of the measurements. The worst strategy is the global one, 2, and the best one is the ST-local reshuffling 4, which is to the best of our knowledge not yet employed in existing QMC codes. One can readily observe the reduction in the intensity of spikes in the comparison of the three schemes in Fig. 1.

Below, we first consider a toy model that mimics all important properties of the QMC partition function 1. It demonstrates the reduction of spikes depending upon the synchronization between measurements and Monte Carlo updates. In the section III we describe the formalism we use for our QMC examples and discuss the links between spikes, fat-tail distributions and zeros of the determinant. In section IV we demonstrate the reduction of spikes depending on the measurement scheme in real-world QMC calculations, giving also some estimates for possible speedup. The conclusion section IV is devoted to discussions and further perspectives. We include two appendices, that discuss the details of the error estimate for fat tailed distributions (Appendix A) as well as a proof showing the link between the power law of the fat-tail distribution for the observables and the dimensionality of the manifold of the field configurations where the fermion determinant vanishes (Appendix B).

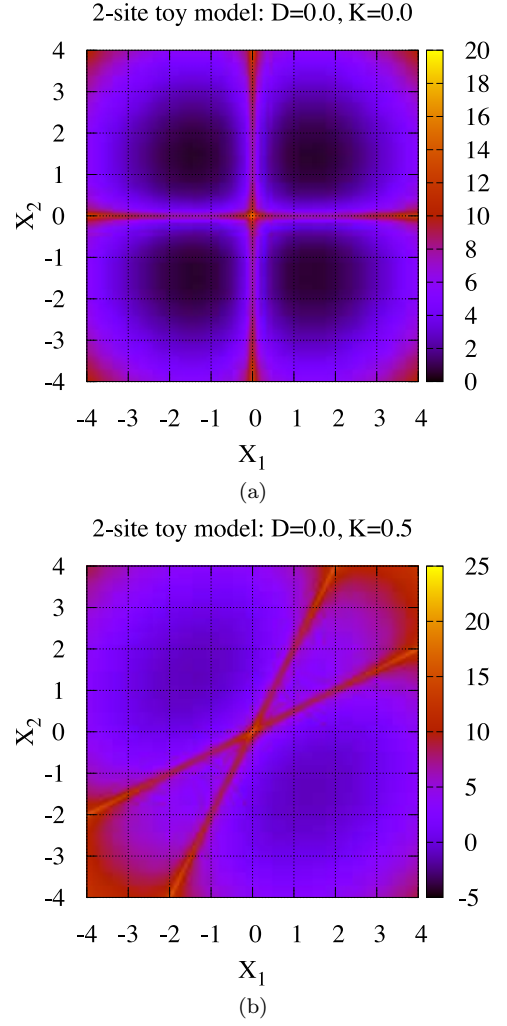


FIG. 2. Action of the two-dimensional toy model 6. Upper plot shows the action when $K = 0.0$ and the fields x_1 and x_2 are uncorrelated. Bottom plot corresponds to $K = 0.5$. $D = 0.0$ in both cases.

II. TOY MODEL

Our toy model is inspired by the recent study of the structure of the path integral within the Lefschetz thimbles approach [12]. We start from the probability distribution for two random variables x_1 and x_2 :

$$P(x_1, x_2) = C_0 e^{-\frac{1}{2}(x_1^2 + x_2^2)} (x_1 - f(x_2))^2 (x_2 - f(x_1))^2, \quad (5)$$

where C_0 is the normalization coefficient. It corresponds to the exponent in the partition function 1, thus the model action can be written as

$$S(x_1, x_2) = \frac{1}{2}(x_1^2 + x_2^2) - 2 \ln |(x_1 - f(x_2))(x_2 - f(x_1))|. \quad (6)$$

The action is symmetrical with respect to the exchange $x_1 \leftrightarrow x_2$, which reflects the translational symmetry of the real lattice models. $P(x_1, x_2)$ includes the Gaussian part

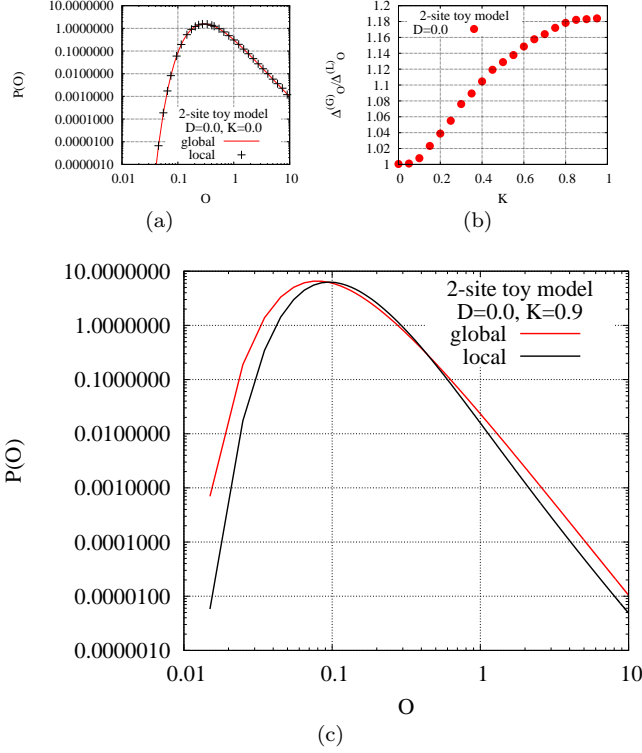


FIG. 3. Results for the toy model: top left figure shows the identical probability distributions for the observable when global or local measurements are used in the case of uncorrelated fields x_1 and x_2 ($K = 0$). Bottom figure is the comparison of the probability distributions for local and global measurements at $K = 0.9$. Top right figure shows the ratio of the widths of the distributions for global and local schemes of measurements (see Eq. 20). Larger value of this ratio corresponds to bigger advantage from local measurements. $D = 0.0$ in all cases.

and the remaining terms model fermion determinants. This structure is inspired by the Hubbard-Stratonovich decomposition with continuous auxiliary fields routinely employed in determinantal QMC [6, 14, 15] (see section III below for the detailed explanation). Our toy "determinants" are equal to zero along the lines $x_1 = f(x_2)$ and $x_2 = f(x_1)$, and we need the second power of each multiplier since there are two equivalent fermion determinants for electrons and holes on a bipartite lattice at half-filling.

The observables should model the fermionic green functions, thus we consider two expressions

$$O_1(x_1, x_2) = \frac{1}{(x_1 - f(x_2))^2}, \quad (7)$$

$$O_2(x_1, x_2) = \frac{1}{(x_2 - f(x_1))^2}, \quad (8)$$

connected with each other through the "translational symmetry" $O_1(x_1, x_2) = O_2(x_2, x_1)$. Average over lattice is equivalent to the computation of the sum $O = \frac{1}{2}(O_1 + O_2)$. Importantly, and as in determinantal QMC

observables diverge at the zeros of the toy determinant.

In order to be able to derive all probability distributions analytically, we consider a linear form $f(x) = D + Kx$. Despite simplicity, this is enough to demonstrate all essential phenomena leading to the reduction of the tail in fat-tailed distributions. The action 6 is plotted in Fig. 2 for two cases: $K = 0, D = 0$, when the two variables are independent, and for $K = 0.5, D = 0$. One can clearly observe the lines, where the action diverges logarithmically. These are the lines corresponding to the zeros of fermion determinant.

The global scheme of measurements is modelled by the following procedure: first, we generate both variables x_1, x_2 according to the probability density 5; second, we measure the full observable O . After transition from the probability distribution 5 for x_1 and x_2 to the probability density $P_O(z)$ for the full observable O we get the following expression:

$$P_O^{(G)}(z) = \frac{C_0}{2} \sum_{\nu_1, \nu_2} \int_{-z}^z d\alpha \frac{e^{-\frac{1}{2}(x_1(z, \alpha, \nu_1, \nu_2)^2 + x_2(z, \alpha, \nu_1, \nu_2)^2)}}{(z - \alpha)^{5/2}(z + \alpha)^{5/2}(1 - K^2)}, \quad (9)$$

where

$$x_1 = \frac{1}{1 - K^2} \left(\frac{\nu_1}{\sqrt{z - \alpha}} + \frac{K\nu_2}{\sqrt{z + \alpha}} + D(K + 1) \right) \\ x_2 = \frac{1}{1 - K^2} \left(\frac{K\nu_1}{\sqrt{z - \alpha}} + \frac{\nu_2}{\sqrt{z + \alpha}} + D(K + 1) \right) \quad (10)$$

and $\nu_{1,2} = \pm 1$. α parametrizes the curve of constant observable O in (x_1, x_2) plane. For simplicity, we considered only the case $K \in (0; 1)$.

In the local scheme of measurements, we compute observable O_1 after the update of x_1 field according to the conditional probability $P(x_1|x_2)$, defined as

$$P(x_1|x_2) = e^{-\frac{1}{2}x_1^2} \times (x_1 - f(x_2))^2 (x_2 - f(x_1))^2 \tilde{C}_0(x_2), \quad (11)$$

with the additional normalization constant $\tilde{C}_0(x_2)$

$$\tilde{C}_0^{-1}(x_2) = \int_{-\infty}^{\infty} d\tilde{x}_1 e^{-\frac{1}{2}\tilde{x}_1^2} (\tilde{x}_1 - f(x_2))^2 \times (x_1 - f(\tilde{x}_1))^2. \quad (12)$$

Subsequently, measurement of O_2 is made after similar update of the x_2 field according to the conditional probability $P(x_2|x_1)$.

In order to derive the probability distribution for the observable, we consider the full Markov sequence in the Monte Carlo process. The sequence of configurations consists of some fixed starting point $x_1^{(0)}$ and values of the fields after subsequent updates: $x_2^{(0)}, x_1^{(1)}, x_2^{(1)}, \dots$. Probability distribution for the full chain of $2N + 1$ local updates can be written as:

$$P_{2N+1}(x_1^{(0)}, x_2^{(0)}, x_1^{(1)}, x_2^{(1)}, \dots, x_1^{(N)}, x_2^{(N)}) = \\ P(x_2^{(0)}|x_1^{(0)}) \prod_{i=1}^N \left(P(x_1^{(i)}|x_2^{(i-1)}) P(x_2^{(i)}|x_1^{(i)}) \right), \quad (13)$$

where each local update is made with the conditional probability 11. According to this notation, O_1 is measured using $(x_1^{(N)}, x_2^{(N-1)})$ pair of fields and O_2 is measured using $(x_1^{(N)}, x_2^{(N)})$ fields.

Due to the fact that the probability 5 is the stationary distribution for this Markov chain, the distribution of the pair $(x_1^{(N)}, x_2^{(N-1)})$ converges to Eq. 5 in the limit $N \rightarrow \infty$:

$$\int dx_2^{(0)} dx_1^{(1)} \dots dx_1^{(N-2)} dx_2^{(N-2)} dx_1^{(N-1)} \times P_{2N-1}(x_1^{(0)}, x_2^{(0)} \dots x_1^{(N-1)}, x_2^{(N-1)}) \times P(x_1^{(N)} | x_2^{(N-1)})|_{N \rightarrow \infty} = P(x_1^{(N)}, x_2^{(N-1)}). \quad (14)$$

Thus, after a sufficiently long warm-up Monte Carlo time, the local measurement scheme can be described as the computation of the observable O , which is a function of three random variables:

$$O(x_1, x_2, \tilde{x}_2) = \frac{1}{2} \left(\frac{1}{(x_1 - f(x_2))^2} + \frac{1}{(\tilde{x}_2 - f(x_1))^2} \right). \quad (15)$$

These variables are distributed according to the probability density

$$P^{(L)}(x_1, x_2, \tilde{x}_2) = P(x_1, x_2)P(\tilde{x}_2|x_1). \quad (16)$$

The final probability distribution for the observable O from 15 reads as

$$P_O^{(L)}(z) = \sum_{\nu=\pm 1} \int_0^\infty d\beta \int_{f(\beta)+1/\sqrt{2z}}^\infty d\alpha C_0 \tilde{C}_0(\alpha) \times e^{-\frac{1}{2}(\alpha^2 + \beta^2 + \tilde{x}_2^2(\alpha, \beta, \nu))} (\alpha - f(\beta))^2 (\beta - f(\alpha))^2 \times (\tilde{x}_2(\alpha, \beta, \nu) - f(\alpha))^2 \frac{\alpha - f(\tilde{x}_2(\alpha, \beta, \nu))}{\left(2z - \frac{1}{(\alpha - f(\beta))^2}\right)^{3/2}}, \quad (17)$$

where

$$\tilde{x}_2(\alpha, \beta, \nu) = f(\alpha) + \nu \left(2z - \frac{1}{(\alpha - f(\beta))^2} \right)^{-1/2} \quad (18)$$

and the pair (α, β) parametrizes the surface of constant observable O in 3D space $(x_1; x_2; \tilde{x}_2)$.

Both distributions have power law asymptotic in the limit $O \rightarrow \infty$:

$$P_O^{(L/G)}(z)|_{z \rightarrow \infty} \approx A^{(L/G)}(D, K)/z^{\xi(D, K)}, \quad (19)$$

where the power ξ stays the same but the prefactors A are different. $P_O^{(L)}(z)$ and $P_O^{(G)}(z)$ are plotted in Fig. 3. First we check that the local and global schemes are identical in case when $K = 0$ (see Fig. 3(a)). Since x_1 and x_2 are completely independent in this case, and O_i is dependent only on corresponding x_i , the order of updates and measurements does not matter. Indeed, the

points for local and global schemes overlap precisely in Fig. 3(a). The situation changes at $K \neq 0$. The example plot for $K = 0.9$ shows that $P_O^{(L)}(z)$ and $P_O^{(G)}(z)$ are now different: both distributions still have the same power law tail which is evident from the double logarithm plot, but the prefactor A is slightly smaller for the local scheme.

In order to quantify this difference, we compute the width of the distribution at the 95% level (see Appendix A):

$$\Delta_O^{(L/G)} = z_2^{(L/G)} - z_1^{(L/G)}, \quad (20)$$

where

$$\int_{z_2^{(L/G)}}^\infty dz P_O^{(L/G)}(z) = 0.025, \quad (21)$$

$$\int_0^{z_1^{(L/G)}} dz P_O^{(L/G)}(z) = 0.025 \quad (22)$$

The ratio $\Delta_O^{(G)}/\Delta_O^{(L)}$ is displayed in Fig. 3(b) depending on K at $D = 0$. We can reach approximately 20% reduction of the tail in the local scheme of measurements.

In the toy model, the improvement is minuscule. We interpret this in terms of the small difference between local and global updates in this two-fields system: even in the local scheme we still update half of the fields. However, as we demonstrate further below, the effectiveness of the tail suppression grows with the dimensionality of the configuration space. Hence the effect becomes quite pronounced in real QMC calculations, where the number of the fields can easily exceed 10^4 .

III. FORMALISM FOR THE REPULSIVE HUBBARD MODEL.

Example QMC calculations will be carried out for the repulsive Hubbard model on bipartite hexagonal and square lattices:

$$\hat{H} = -t \sum_{\langle i, j \rangle, \sigma} \hat{c}_{i, \sigma}^\dagger \hat{c}_{j, \sigma} + U \sum_i (\hat{n}_{i, \uparrow} - 1/2)(\hat{n}_{i, \downarrow} - 1/2). \quad (23)$$

Here, $\hat{c}_{i, \sigma}^\dagger$ are creation operators for electrons with spin $\sigma = \uparrow, \downarrow$ at site i and $\hat{n}_{i, \sigma} = \hat{c}_{i, \sigma}^\dagger \hat{c}_{i, \sigma}$. It is beyond the scope of this article to provide a detailed review of the finite temperature auxiliary field QMC algorithm and we refer the reader to Refs. [6, 8] for overviews and implementations of the algorithm. Here we will concentrate on the so called SU(2) invariant Hubbard-Stratonovich (HS) transformation [16]. In order to introduce it, we carry out a partial particle-hole transformation,

$$\begin{cases} \hat{c}_{i, \uparrow}, \hat{c}_{i, \uparrow}^\dagger \rightarrow \hat{a}_i, \hat{a}_i^\dagger, \\ \hat{c}_{i, \downarrow}, \hat{c}_{i, \downarrow}^\dagger \rightarrow \pm \hat{b}_i^\dagger, \pm \hat{b}_i \end{cases}, \quad (24)$$

where the sign in the second line alternates depending on the sublattice, \hat{a}_i^\dagger and \hat{b}_i^\dagger are creation operators for

electrons and holes correspondingly. The Hamiltonian [23](#) acquires the following form:

$$\hat{H} = -t \sum_{\langle i,j \rangle} (\hat{a}_i^\dagger \hat{a}_j + \hat{b}_i^\dagger \hat{b}_j) + \frac{U}{2} \sum_i \hat{q}_i^2, \quad (25)$$

where $\hat{q}_i = \hat{a}_i^\dagger \hat{a}_i - \hat{b}_i^\dagger \hat{b}_i$ is the operator of electrical charge measured with respect to the half-filled case on site i .

In order to make an analytical prediction on the power law in the heavy-tailed distributions, we need to introduce the continuous auxiliary fields on the basis of the usual Gaussian HS transformation:

$$e^{-\frac{\Delta\tau}{2} U \hat{q}^2} \cong \int D\phi e^{-\frac{1}{2U\Delta\tau} \phi^2} e^{i\phi\hat{q}}. \quad (26)$$

The partition function can be obtained as the integral

$$\mathcal{Z} = \int \mathcal{D}\phi_{i,\tau} e^{-S_B} \det M_{el.} \det M_{h.},$$

$$S_B(\phi_{i,\tau}) = \sum_{i,\tau} \frac{\phi_{i,\tau}^2}{2\Delta\tau U}, \quad (27)$$

where fermionic operators for continuous auxiliary fields are written as

$$M_{el.} = I + \prod_{\tau=1}^{L_\tau} (e^{-\Delta\tau h} \text{diag} (e^{i\phi_{i,\tau}})),$$

$$M_{h.} = I + \prod_{\tau=1}^{L_\tau} (e^{-\Delta\tau h} \text{diag} (e^{-i\phi_{i,\tau}})). \quad (28)$$

Both fermionic operators are $V \times V$ matrices where V is the number of lattice sites in space, h is the matrix of single-particle Hamiltonian which defines the tight-binding part in the expression [25](#). The diagonal $V \times V$ matrix $\text{diag} (e^{-i\phi_{i,\tau}})$ includes all exponents with auxiliary fields belonging to a given Euclidean time slice τ . From Eq. [27](#) we conclude that the full action includes both quadratic form and the logarithms of the fermion determinants, pretty similar to the toy model [6](#):

$$S = S_B - \ln(\det M_{el.} \det M_{h.}). \quad (29)$$

In practical QMC calculations, the exponent [26](#) is replaced by the Gauss-Hermite quadrature up to fourth order [\[17\]](#):

$$e^{-\Delta\tau \frac{U}{2} \hat{q}_i^2} = \sum_{s=\pm 1, \pm 2} \gamma(s) e^{i\lambda\eta(s)\hat{q}_i} + \mathcal{O}\left\{(\Delta\tau U)^4\right\} \quad (30)$$

with $\lambda = \sqrt{\Delta\tau U/2}$, $\gamma(\pm 1) = 1 + \sqrt{6}/3$, $\gamma(\pm 2) = 1 - \sqrt{6}/3$ and $\eta(\pm 1) = \pm\sqrt{2(3 - \sqrt{6})}$, $\eta(\pm 2) = \pm\sqrt{2(3 + \sqrt{6})}$ [\[8\]](#).

In this case the partition function can be computed as a sum over all possible values of discrete fields $s_{i,\tau}$:

$$\mathcal{Z} = \sum_{s_{i,\tau}} \prod_{i,\tau} \gamma(s_{i,\tau}) \det D_{el.}(s_{i,\tau}) \det D_{h.}(s_{i,\tau}), \quad (31)$$

where $D_{el.}$ and $D_{h.}$ are the fermionic operators for electrons and holes respectively:

$$D_{el.}(s_{i,\tau}) = I + \prod_{\tau=1}^{L_\tau} \left(e^{-\Delta\tau h} \text{diag} \left(e^{i\lambda\eta(s_{i,\tau})s_{i,\tau}} \right) \right),$$

$$D_{h.}(s_{i,\tau}) = I + \prod_{\tau=1}^{N_t} \left(e^{-\Delta\tau h} \text{diag} \left(e^{-i\lambda\eta(s_{i,\tau})s_{i,\tau}} \right) \right) \quad (32)$$

For the details of sampling algorithms and calculation of observables, we refer a reader to the description of ALF package [\[8\]](#). Despite quite different expression for the partition function, we get quite similar results for discrete and continuous fields if the sampling algorithms are equivalent (see numerical proof and discussion in the end of the section [IV](#)).

In our examples, we consider four different observables:

- Sublattice charge fluctuations:

$$\hat{Q}^2 = \left(\sum_{i \in \text{sublat.1}} \hat{q}_i \right)^2 \quad (33)$$

- Sublattice spin fluctuations:

$$\hat{S}^2 = \left(\sum_{i \in \text{sublat.1}} (\hat{n}_{i,\uparrow} - \hat{n}_{i,\downarrow}) \right)^2 \quad (34)$$

- Double occupancy:

$$\hat{d} = \frac{1}{V} \sum_i \hat{n}_{i,\uparrow} \hat{n}_{i,\downarrow} \quad (35)$$

- squared staggered moment:

$$\Delta \hat{S}^2 = \left(\sum_{i \in \text{sublat.1}} (\hat{n}_{i,\uparrow} - \hat{n}_{i,\downarrow}) - \sum_{i \in \text{sublat.2}} (\hat{n}_{i,\uparrow} - \hat{n}_{i,\downarrow}) \right)^2 \quad (36)$$

All these observables include the second powers of equal-time fermion green function g_τ . Due to the relation

$$\det g_\tau^{-1} = \det D_{el.}, \quad (37)$$

which also holds for continuous auxiliary fields, $\det g_\tau$ (thus at least some elements of the green function g_τ itself) diverges at zeros of the determinant. These divergences are the reason why the distributions of four-fermion observables become heavy-tailed, as observed in the toy model [19](#). As shown in Appendix [B](#), the power ξ can be connected to the dimensionality of the manifolds, on which the determinants vanish. The SU(2) invariant HS decomposition for the Hubbard model corresponds to the worst-case scenario [\[12\]](#). Here, the zeros of the determinant form "domain walls" in configuration space such that the dimensionality the zero-manifolds is given

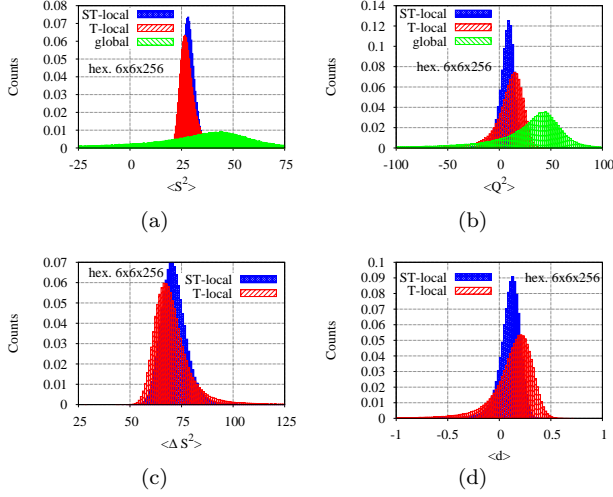


FIG. 4. Histograms for the distribution of observables after one full sweep. Each plot corresponds to one observable (top left - sublattice spin fluctuations, top right - sublattice charge fluctuations, bottom left - squared staggered moment, bottom right - double occupancy). In each case several ways of synchronization between updates and calculation of observable are shown. Calculations were done on the $6 \times 6 \times 256$ hexagonal lattice at $U = 5.0$ and $\beta = 20.0$ using the SU(2) symmetrical discrete HS field with standard local Blankenbecler, Scalapino, Sugar (BSS)-QMC updates.

$VL_\tau - 1$, where VL_τ corresponds to the number of auxiliary fields. The connection to the power law in heavy-tailed distributions was considered in details in [18] and for the particular case of zeros of the determinant forming domain walls, $\xi = 5/2$. A detailed proof is given in Appendix B.

IV. QMC RESULTS

We carried test calculations on several lattices:

- 6×6 hexagonal lattices with $L_\tau = 256$ and $L_\tau = 512$ at the same temperature to test the influence of the step in Euclidean time;
- 12×12 hexagonal lattice with $L_\tau = 256$;
- 8×8 square lattice with $L_\tau = 256$;

For all our calculations, we have fixed the strength of Hubbard interaction to $U = 5.0$ in units of the hopping matrix element and set the inverse temperature to $\beta = 20.0$.

We consider the three schemes of synchronization of updates and measurements, described in the Introduction. The double occupancy 35 is a local observable, thus the expressions 2, 3 and 4 are fully applicable. Other observables are only local in Euclidean time, but contain spatial correlations $\hat{O}_{i,\tau}\hat{O}_{j,\tau}$. In this case, global and

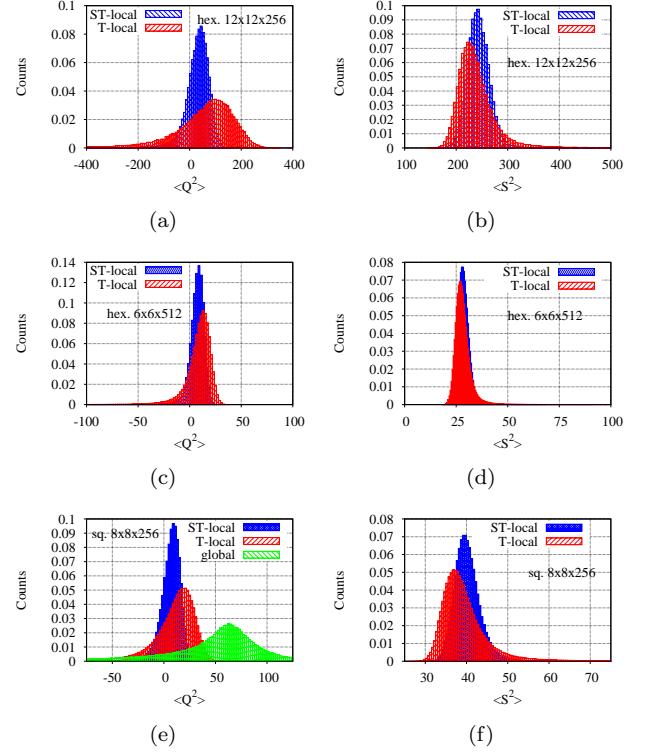


FIG. 5. Comparison of the distribution of observables for different lattices and models: left (right) column shows sublattice charge (spin) fluctuations. First (upper) row corresponds to a $12 \times 12 \times 256$ hexagonal lattice, the second row shows the results for the $6 \times 6 \times 512$ hexagonal lattice with a twice smaller step in Euclidean time and the third row corresponds to the square lattice Hubbard model on the $8 \times 8 \times 256$ lattice. The Hubbard interaction and temperature are the same in all cases: $U = 5.0$ and $\beta = 20.0$. For comparison with the $6 \times 6 \times 256$ lattice, one can refer to the upper row in Fig. 4.

T-local schemes are essentially the same as for local observables: in the former case, we compute all correlators at all time slices after updating all fields; in the latter case, all correlators on time slice τ are computed after updating all fields in the same time slice. The ST-local scheme is slightly modified: we compute the average for the correlator $\hat{O}_{i,\tau}\hat{O}_{j,\tau}$ after local updates of both the fields $s_{i,\tau}$ and $s_{j,\tau}$. Since we need all possible correlators of spin and charge to measure the observables 33, 34 and 36, we in practice simply update the average for $\hat{O}_{i,\tau}\hat{O}_{j,\tau} \forall j$ (with \hat{O} representing operator of local spin or charge) after each local update of the $s_{i,\tau}$ field.

We start from the histograms for the distributions of observables. In all cases we take the averages over the full lattice volume after one full sweep of local updates through the field configuration, with corresponding synchronization between updates and measurements. All four observables presented in Fig. 4 are computed on $6 \times 6 \times 256$ lattices. Distributions for $\langle S^2 \rangle$ and $\langle \Delta S^2 \rangle$ have heavy tails towards $+\infty$ and the distributions for double occupancy and $\langle Q^2 \rangle$ have heavy tails towards $-\infty$. The

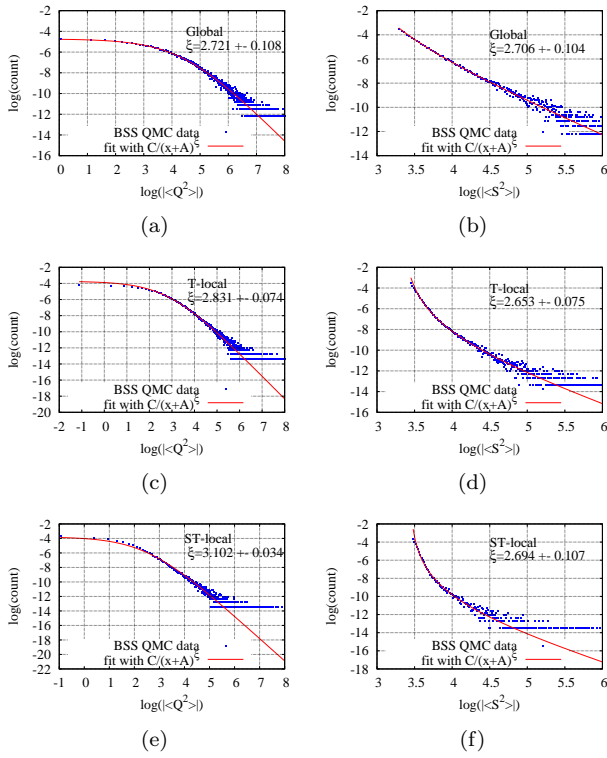


FIG. 6. Fit of the tail of the histograms to the form $\frac{C}{(x+A)^\xi}$. Left (right) column shows the sublattice charge (spin) fluctuations. First (upper) row corresponds to the global measurement of an observable, the second row shows the T-local computations and the last (lower) row corresponds to the ST-local scheme of measurement. All data were produced on the $6 \times 6 \times 256$ lattice at $U = 5.0$ and $\beta = 20.0$.

differences between global, T-local and ST-local schemes are quite noticeable with the width of the distributions decreasing with synchronization of measurements and updates. We are mostly interested in the comparison of ST-local and T-local schemes, since the former one offers some improvement for existing QMC codes [8]. Distributions for double occupancy, $\langle Q^2 \rangle$ (Fig. 4(d) and 4(b)) shows a notable improvement when considering an ST-local scheme as opposed to a T-local one. On the other hand, the improvement is smaller for non-local observables such as the spin-spin correlations, Fig. 4(a) and 4(c).

Comparison of the distributions on different lattices (Fig. 5) shows that the effect increases for larger lattices. This becomes apparent when one compares the differences between ST-local and T-local histograms of Figs. 4(b) and 5(a). In contrast, the effect decreases with decreasing step in Euclidean time. In particular, the ST-local and T-local histograms are closer to each other in Fig. 5(c) than in Fig. 4(b). This can be attributed to the decreasing influence of the single local update in the continuum limit. Results for the square lattice also demonstrate a somewhat increased difference between ST-local and T-local measurements on lattices

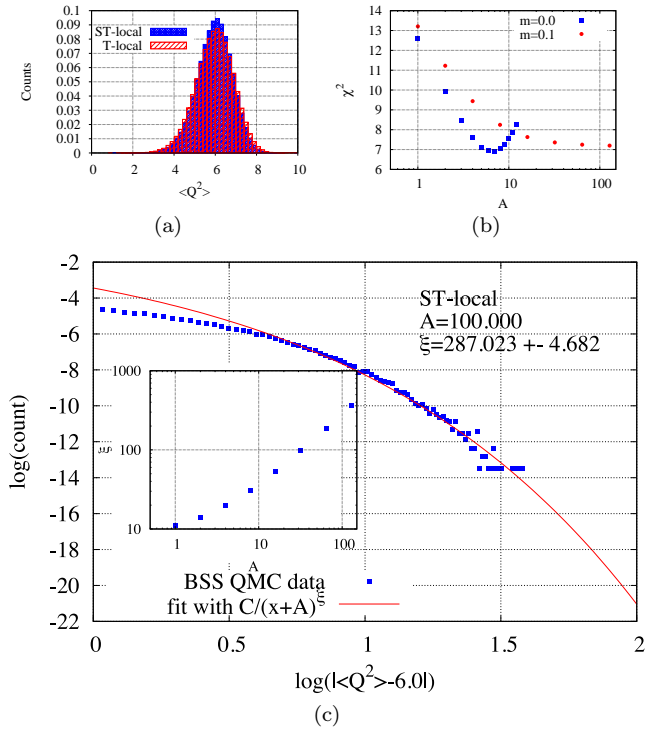


FIG. 7. Top left figure: histogram for the distribution of the sublattice charge fluctuations in the calculation with the staggered mass, that eliminates the zeros of the determinant. Bottom figure: an attempt to fit the tail of the histogram by a power law (at fixed shift parameter A). The inset shows the steady increase of the power in the fit upon increasing A . Top right figure shows the dependence of χ^2 on the shift A for two different cases: with and without the staggered mass term. The computations were carried out on a $6 \times 6 \times 256$ lattice at $\beta = 20$, $U = 5$, and mass $m = 0.1$.

of similar size; compare Fig. 5(f) for the $8 \times 8 \times 256$ square lattice and Fig. 4(a) for the $6 \times 6 \times 256$ hexagonal lattice.

In Fig. 6 we fit the tails of the histograms for our considered observables and measurement schemes to the form $\frac{C}{(x+A)^\xi}$. Within our error-bars, ξ is independent on the measurement scheme, and is reasonably close to the theoretical value $5/2$. The difference may be explained by the presence of lower-dimensional manifolds in the configurations space, formed by the intersection of "domain walls" of zeros of the determinant. They can result in higher-order power law corrections to the asymptotic, that are quite hard to detect in the noisy numerical data.

One can get rid of the zeros of the determinant by breaking symmetries in the form of mass terms. A possible choice is to add to the quantum Hamiltonian Eq. 23 the term

$$\hat{H}_m = m \sum_{i \in \text{sublat.1}} (n_{i,\uparrow} - n_{i,\downarrow}) + m \sum_{i \in \text{sublat.2}} (n_{i,\downarrow} - n_{i,\uparrow}). \quad (38)$$

that breaks $SU(2)$ spin symmetry. It is known [19] that this mass term in conjunction with our choice of the HS

transformation removes the zeros from the fermion determinant. Fig. 7(a) plots the histograms in the presence of the mass term. As apparent, the differences between the measurement schemes disappear. The absence of the heavy tails in this case can be proven if we attempt to fit the tails of the finite mass histograms with a power law. This fit never converges: there is no local minimum of χ^2 with respect to the shift parameter A in the power law

$$P_O^{(L/G)}(z)|_{z \rightarrow \infty} \approx C/(z + A)^\xi. \quad (39)$$

Figure 7(b) clearly outlines this difference between finite m and zero m data. Consequently, both the shift A and the power ξ grow indefinitely in the fitting procedure (see the inset on Fig. 7(c)), thus demonstrating that the power law is incompatible with the finite mass data.

This analysis allows for the claim that the heavy tails and concomitant reduction of the observed spikes in various measurement schemes is entirely caused by the zeros of the fermion determinant.

We now compare *error bars* for different measurement schemes. Since the second moment of the distribution is not defined for tails with $\xi \approx 5/2$, the central limit theorem is not applicable and we need to resort to more elaborate error estimation algorithms. For a given simulation consisting of N sweeps with N exceeding the auto-correlation time, we repeat it for up to several thousand times and study the properties of distributions for the averages obtained during the individual simulations. The details of this analysis are described in Appendix A. Here we present the results for the 95% confidence interval for the averages depending upon the number of sweeps per simulation. Since our different schemes only reshuffle measurements, they come at the same computational cost. Hence the comparison between measurements schemes is carried out at equal computational time.

Curves for all three measurement schemes are shown in Fig. 8 for the sublattice spin and charge fluctuations computed on the $6 \times 6 \times 256$ hexagonal lattice. In general, the error bars reflect the relation between the widths of the histograms for different measurement schemes. The global scheme stands out and is always at a big disadvantage: the error bar is at least an order of magnitude larger in comparison to the ST-local scheme. The ST-local scheme also offers an improvement in the error bars by a factor $2 \dots 3$ in comparison with T-local scheme. We foresee that this improvement will be more pronounced on larger lattices. Fig. 8 shows the results for the relatively small $6 \times 6 \times 256$ lattice, and plots for larger lattices can be found in Appendix A.

The scaling of the errors with the number of sweeps per simulation is also different for different schemes. Insets in the figures 8(a) and 8(b) show the power law fit for this scaling, where the error bar is proportional to $1/N_{\text{sweeps}}^\mu$. At the onset, we notice that the errors decrease slower than $N_{\text{sweeps}}^{-1/2}$, thereby reflecting the invalidity of the central limit theorem. The power is consistently higher for the ST-local scheme. Thus the error

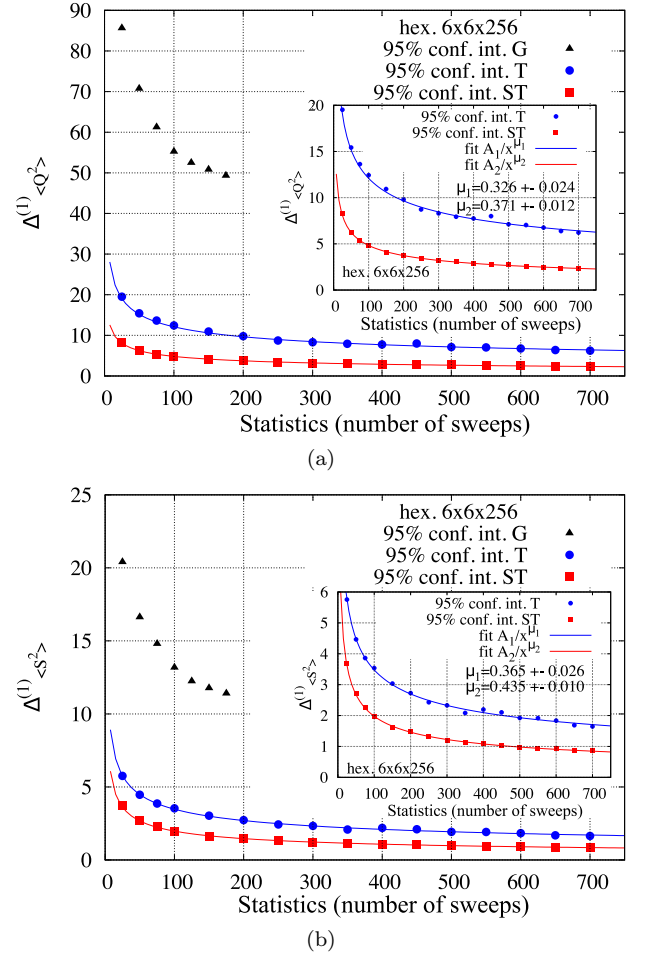


FIG. 8. Comparison of error bars (width of the 95% confidence interval) for different algorithms depending on the number of sweeps per simulation. We have adjusted the vertical axis to accommodate all three algorithms: global, T-local and ST-local measurements. The top (bottom) plot shows the results for the sublattice charge (spin) fluctuations. The data set was produced on a $6 \times 6 \times 256$ hexagonal lattice at $U = 5.0$ and $\beta = 20.0$. Here, the staggered mass is equal to zero. Insets in both plots show the same data, but the vertical scale adjusted to include only the T-local and ST-local algorithms.

bar decreases faster for ST-local measurements and the speedup increases with decreasing tolerance on the size of the error bar.

Using these fits we can estimate the speedup for a given relative error for various observables. Conservative estimates, based on the fastest (within the error bars) decrease of confidence interval for T-local scheme and the slowest decrease of the confidence interval for the ST-local scheme are shown in Fig. 9. As expected, the largest effect is observed for the local quantity, the double occupancy. In this case the speedup can reach up to two orders of magnitude if we demand the relative error to be less than 1%. However, even for other observables which contain some spatial correlators, the speedup is quite substantial and varies from 5 to 10.

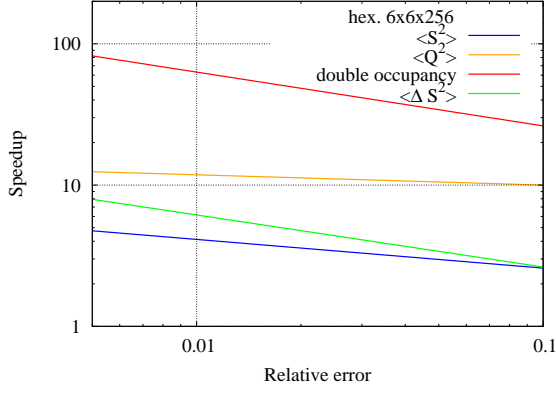


FIG. 9. Conservative estimate of the speedup: we take the maximal value within the error bars for the power law coefficient μ in case of the T-local measurements and the minimal value of μ for the ST-local measurements. The speedup is estimated at fixed relative error of the corresponding observable. Data for the power law fits are taken from Fig. 8 and A.3, such that the speedup pertains to simulations on the $6 \times 6 \times 256$ hexagonal lattice at $U = 5.0$ and $\beta = 20.0$. Here, the staggered mass is equal to zero.

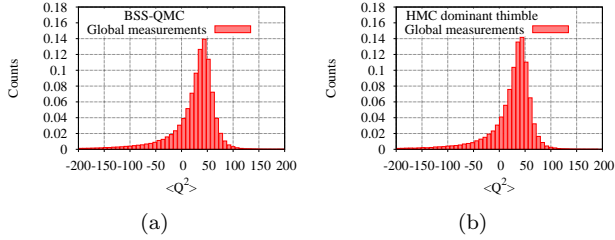


FIG. 10. Comparison of the histograms for the sublattice charge fluctuations obtained in QMC calculations with discrete and continuous auxiliary fields. Left plot corresponds to the SU(2) symmetrical discrete fields updated using standard local BSS QMC updates. Right plot corresponds to the SU(2) symmetrical continuous fields, updated with the Hybrid Monte Carlo algorithm constrained in the dominant thimble [20]. In both cases we employ global measurements: observables are computed on the whole lattice after the update of all fields. Computations were done on a $6 \times 6 \times 256$ at $\beta = 20$ and $U = 5$.

The effectiveness of the ST-local scheme for the double occupancy can be qualitatively understood by looking into the details of local updates in BSS-QMC. For the specific choice of the HS transformation 30, and at the considered particle-hole symmetric case, the ratio of new to old weight upon changing the auxiliary field at space-time site \mathbf{i}, τ from $s_{\mathbf{i}, \tau}$ to $\tilde{s}_{\mathbf{i}, \tau}$ reads:

$$R_{\mathbf{i}, \tau} = \frac{\gamma(\tilde{s}_{\mathbf{i}, \tau})}{\gamma(s_{\mathbf{i}, \tau})} |(1 - E_{\mathbf{i}, \mathbf{i}}(\tau))G_{\mathbf{i}, \mathbf{i}}(\tau) + E_{\mathbf{i}, \mathbf{i}}(\tau)|^2, \quad (40)$$

where

$$E_{\mathbf{i}, \mathbf{i}}(\tau) = e^{i\lambda\eta(\tilde{s}_{\mathbf{i}, \tau})\tilde{s}_{\mathbf{i}, \tau} - i\lambda\eta(s_{\mathbf{i}, \tau})s_{\mathbf{i}, \tau}}. \quad (41)$$

As a consequence, if the Green function takes a large value, due to proximity of a zero of the determinant, the flip will be accepted, and the configuration will be *re-pelled* from the zero mode. Observables such as the double occupancy that rely only on the knowledge of $G_{\mathbf{i}, \mathbf{i}}(\tau)$, after the update has been carried out, are hence expected to show less fluctuations. Generally speaking, the performance of the ST-local synchronization scheme lies in the effectiveness of the local updates in driving the field configurations away of zeros of determinant, and in the fact that the local observable $O_{\mathbf{i}, \tau}(C)$ is mostly dependent on the local fields $s_{\mathbf{i}, \tau}$.

Finally, we address the question of the dependence of our findings on the choice of the HS transformation: continuous, Eq. 26, or discrete, Eq. 30. Since the step from continuous to discrete is provided by the Gauss-Hermite quadrature [17], we can conjecture that in the small imaginary time step limit, $\Delta\tau \rightarrow 0$, both discrete and continuous HS transformation will yield identical fat tailed distributions. We however carry out our simulations at finite imaginary time step such that further comparison is required between simulations based on continuous fields, such as Hybrid Monte Carlo (HMC), and those based on discrete ones. It is well-known [11, 12] that HMC is not ergodic for the SU(2)-invariant continuous HS transformation for the Hubbard model due to above mentioned domain walls formed by zeros of the determinant. However, it turns out that an extremely good approximation is obtained when the simulation is started at the dominant saddle point. We refer the interested reader to Refs. [12, 20] for a full account of this so called *dominant thimble* approximation. In Fig. 10 we compare the distributions obtained from the HMC within the *dominant thimble* approximation and for the discrete fields. The distributions are almost identical, thus providing evidence that the impact of the zeros of the determinant on the distribution is independent of the choice of the HS transformation.

CONCLUSION

We introduced a simple trick to reduce the prefactor of heavy-tailed distributions appearing in fermion QMC simulations when zeros in the fermion determinant occur. The algorithm relies on the synchronization of Monte Carlo updates and measurements of observables. In particular, our strategy is to measure all observables containing the fermionic propagators with source or sink at site (\mathbf{i}, τ) *immediately* after the local update of the auxiliary field on this site. This reshuffling of the measurements suppresses spikes in observables. As a consequence, the statistical uncertainty is reduced *without* additional computational effort. Impressive results are obtained for local observables, and a moderate speedup is seen for equal time two-point correlations functions such spin fluctuations. It would certainly be interesting to investigate this strategy for time displaced correlation

functions. However, this requires substantial reorganization of the existing QMC code and is left for future work.

As we can see from our toy model, the dependence of the error bars on the synchronization between updates and measurements in the presence of zeros of the fermion determinant is a general phenomena in fermion Monte Carlo. It hinges on the fact that in these methods the determinant of the inverse of the single particle Green function matrix corresponds to the weight of a configuration. The efficiency of the algorithm, in the case of local updates synchronised with local measurements depends on the effectiveness of local updates to drive the field configuration away from zeros of the determinant. It is hard to predict whether the local updates will or will not have this feature for other models. But since the price tag for the implementation of the ST-local scheme is zero it is worth implementing. We also note that in the absence of zeros, as obtained by including a non-zero mass, reshuffling of measurements does not alter the statistics. Hence our reshuffling scheme can only lead to improvements. Let us also note that we have checked on an 8-site 2×2 hexagonal lattice that all three measurement schemes give identical results and compare well to exact diagonalization. We are aware of no arguments against the implementation of the proposed synchronization between updates and measurements in existing QMC codes.

Comparison of the distributions of observables for continuous and discrete fields (Fig. 10) also gives new insight on why simulations with continuous fields suffer

worse statistical fluctuations. The observed improvement in spikes after transfer to discrete fields [11] should not be attributed to the nature of discrete fields themselves, but to the switch from a global to a T-local measurement scheme. This observation will have consequences for the algorithms where the global measurement scheme is the default such as in HMC and Langevin dynamics. Our results show that for such updating schemes, it is beneficial to supplement the e.g. global HMC update with subsequent series of local updates synchronized with the measurement of observables. This idea should however be subject of further investigations, since it is unclear, whether it is possible or not to keep the scaling of the HMC with pseudofermions during these additional local updates.

ACKNOWLEDGMENTS

Computational resources were provided by the Gauss Centre for Supercomputing e.V. (www.gauss-centre.eu) through the John von Neumann Institute for Computing (NIC) on the GCS Supercomputer JUWELS [21] at Jülich Supercomputing Centre (JSC). MU thanks the DFG for partial financial support under the project AS120/14-1. FFA acknowledges financial support from the DFG through the Würzburg-Dresden Cluster of Excellence on Complexity and Topology in Quantum Matter - ct.qmat (EXC 2147, project-id 39085490).

-
- [1] R. Blankenbecler, D. J. Scalapino, and R. L. Sugar, *Phys. Rev.* **D24**, 2278 (1981).
 - [2] G. Sugiyama and S. Koonin, *Annals of Physics* **168**, 1 (1986).
 - [3] S. Duane, A. D. Kennedy, B. J. Pendleton, and D. Roweth, *Phys. Lett.* **B195**, 216 (1987).
 - [4] S. White, D. Scalapino, R. Sugar, E. Loh, J. Gubernatis, and R. Scalettar, *Phys. Rev. B* **40**, 506 (1989).
 - [5] S. Sorella, S. Baroni, R. Car, and M. Parrinello, *Europhysics Letters (EPL)* **8**, 663 (1989).
 - [6] F. Assaad and H. Evertz, in *Computational Many-Particle Physics*, Lecture Notes in Physics, Vol. 739, edited by H. Fehske, R. Schneider, and A. Weiße (Springer, Berlin Heidelberg, 2008) pp. 277–356.
 - [7] H. Shi and S. Zhang, *Phys. Rev. E* **93**, 033303 (2016).
 - [8] ALF Collaboration, F. F. Assaad, M. Bercx, F. Goth, A. Götz, J. S. Hofmann, E. Huffman, Z. Liu, F. Parisen Toldin, J. S. E. Portela, and J. Schwab, [arXiv:2012.11914](https://arxiv.org/abs/2012.11914) (2021), <https://arxiv.org/abs/2012.11914> [cond-mat.str-el].
 - [9] G. G. Batrouni, G. R. Katz, A. S. Kronfeld, G. P. Lepage, B. Svetitsky, and K. G. Wilson, *Phys. Rev. D* **32**, 2736 (1985).
 - [10] A. Goetz, S. Beyl, M. Hohenadler, and F. F. Assaad, (2021), [arXiv:2102.08899](https://arxiv.org/abs/2102.08899) [cond-mat.str-el].
 - [11] S. Beyl, F. Goth, and F. Assaad, *Phys. Rev.* **B97**, 085144 (2018), [arXiv:1708.03661](https://arxiv.org/abs/1708.03661) [cond-mat.str-el].
 - [12] M. Ulybyshev, C. Winterowd, and S. Zafeiropoulos, *Phys. Rev. D* **101**, 014508 (2020).
 - [13] M. Bercx, F. Goth, J. S. Hofmann, and F. F. Assaad, *SciPost Phys.* **3**, 013 (2017), [arXiv:1704.00131](https://arxiv.org/abs/1704.00131).
 - [14] P. Buividovich, D. Smith, M. Ulybyshev, and L. von Smekal, *Phys. Rev.* **B99**, 205434 (2019), [arXiv:1812.06435](https://arxiv.org/abs/1812.06435) [cond-mat.str-el].
 - [15] P. Buividovich, D. Smith, M. Ulybyshev, and L. von Smekal, *Phys. Rev.* **B98**, 235129 (2018), [arXiv:1807.07025](https://arxiv.org/abs/1807.07025) [cond-mat.str-el].
 - [16] J. Hirsch, *Phys. Rev. B* **28**, 4059 (1983).
 - [17] F. Goth, “Higher order auxiliary field quantum monte carlo methods,” (2020), [arXiv:2009.04491](https://arxiv.org/abs/2009.04491) [cond-mat.str-el].
 - [18] M. V. Ulybyshev and S. N. Valgushev, (2017), [arXiv:1712.02188](https://arxiv.org/abs/1712.02188) [cond-mat.str-el].
 - [19] P. V. Buividovich and M. I. Polikarpov, *Phys. Rev. B* **86**, 245117 (2012).
 - [20] M. Ulybyshev and F. Assaad, To be published (2021).
 - [21] Jülich Supercomputing Centre, *Journal of large-scale research facilities* **5** (2019), 10.17815/jlsrf-5-171

Appendix A: Statistical processing of QMC data

In this appendix we describe the statistical analysis of the heavy-tailed Monte Carlo data. To obtain an error estimation on observables measured in simulations with statistics size of N sweeps, we repeat the simulation several times with different random seeds so as to determine the distribution of the average observable for a given simulation. In the absence of fat tails, and provided that the number of sweeps exceeds the autocorrelation time, the distribution will follow a Gauss law as expected from the central limit theorem. As we cannot rely on this theorem some care has to be taken in determining the error. In particular we carry out the following analysis.

- Individual simulations with N sweeps are repeated M times, where M is large enough to study the tails of the averages obtained in individual simulations.
- For any observable O , the average over the whole set of M simulations with N sweeps each is used as an estimate for the "true average" $\langle\langle O \rangle\rangle$.
- For each i -th simulation, we compute average $\langle O \rangle_i$ and variance for all observables.
- Distribution of these individual averages and the variances are used in further error estimation.

The following quantities are used to estimate the error bar:

- 95% confidence interval. Its width $\Delta_O^{(1)}$ is defined by the fact that the true average $\langle\langle O \rangle\rangle$ fits inside 95% of the intervals $(\langle O \rangle_i - (1-r)\Delta_O^{(1)}; \langle O \rangle_i + r\Delta_O^{(1)})$. Since the distributions of observables are highly non-symmetrical, we also use non-symmetrical confidence intervals, with the parameter $r \in (0; 1)$ defining the deviation of the confidence interval from symmetrical form. The width of the confidence interval $\Delta_O^{(1)}$ is optimized using this non-symmetry: we take the value of r , where the width $\Delta_O^{(1)}$ is minimal.
- 95% credible interval. Its width $\Delta_O^{(2)}$ is defined by cutting 2.5% tails of the probability distributions of averages over individual simulations $\langle O \rangle_i$:

$$\Delta_O^{(2)} = z_2 - z_1, \quad (\text{A1})$$

where

$$\int_{z_2}^{\infty} dz P_N(z) = 0.025, \quad (\text{A2})$$

$$\int_{-\infty}^{z_1} dz P_N(z) = 0.025 \quad (\text{A3})$$

and $P_N(z)$ is the probability distribution for individual averages over simulations (each simulation

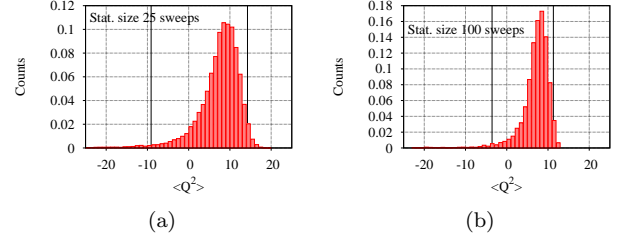


FIG. A.1. Histograms for the distribution of averages of the sublattice charge fluctuations over 25 (left plot) and 100 (right plot) sweeps. Vertical lines show the borders of 95% credible interval obtained from Eq. A3 and A2. Computations were done on the $6 \times 6 \times 256$ lattice at $\beta = 20$ and $U = 5$. T-local measurements were used to compute the observable.

contains N sweeps). In practice, these probability distributions are defined numerically using the histograms plotted for the corresponding data sets. It means that M should be large enough to have enough data points in the tails of these histograms.

- Average variance multiplied by the corresponding Student's t critical value $t_{\infty, 0.025} \approx 1.960$:

$$\Delta_O^{(3)} = 2t_{\infty, 0.025} \frac{1}{M} \sum_{i=1}^M \left(\sqrt{\frac{\sum_{j=1}^N (O_i^j - \langle O \rangle_i)^2}{N(N-1)}} \right), \quad (\text{A4})$$

where O_i^j is the value of observable O for j -th sweep in i -th simulation. In the normal situation, when the central limit theorem holds, this quantity should scale as $1/\sqrt{N}$. In our case, the tails are heavy enough to make the central limit theorem not applicable, and we will see that $\Delta_O^{(3)}$ deviates from this scaling.

Fig. A.1 shows two examples of histograms for the averages over individual simulations. Fig. A.1(a) corresponds to the individual simulations with $N = 25$ sweeps and Fig. A.1(b) corresponds to the simulations with $N = 100$ sweeps. One can see how the probability distribution becomes more narrow, while remaining heavy tailed towards negative values of the observable. Vertical lines in the figures correspond to the borders of the 95% credible interval z_1 and z_2 defined in Eq. A3 and A2. Since the distribution becomes more narrow, the width of the credible interval also decreases from approximately 23.2 for the simulation size 25 to 14.9 for the simulation size 100. However, it does not decrease by two times as expected for the case when the central limit theorem holds.

The dependence of various error bars estimators on the number of sweeps, N , in the simulation is shown in Fig. A.2. In all cases we compare the three measures: confidence interval $\Delta_O^{(1)}$, credible interval $\Delta_O^{(2)}$ and average variation $\Delta_O^{(3)}$. It appears that all three quantities give quite similar estimate for the error bar. The largest dis-

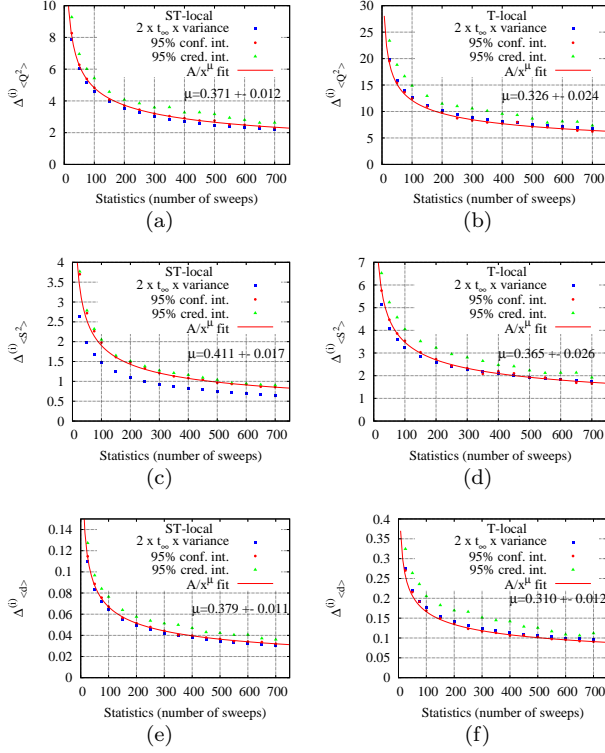


FIG. A.2. Dependence of various error estimates on the number of sweeps per simulation. We consider the 95% confidence interval, the 95% credible interval, and the average variance A4. In all cases we added a power law fit for the confidence interval data set. Left column corresponds to the ST-local measurements and right column corresponds to the T-local measurements. Different rows show the results for different observables: the first (upper) row demonstrates the error bar for the sublattice charge fluctuations, the second row for the sublattice spin fluctuations and the last (bottom) row for the double occupancy. All data was produced on the $6 \times 6 \times 256$ hexagonal lattice at $U = 5.0$ and $\beta = 20.0$. The staggered mass was set to zero.

crepancy is around 30% and it is observed only in the single case of sublattice spin fluctuations for ST-local measurements. In all other cases the discrepancy is smaller than 20% and is typically observed as a deviation of credible interval, while the average variance and confidence interval are in next to perfect agreement. For further consideration we will exclusively use the 95% confidence interval as a measure of the error bar. The coincidence with the average variance allows us to use the variance as an error estimate in realistic situation, when we do not repeat simulations M times in order to directly observe the distribution of averages over individual simulations. Fitting the confidence interval data with the power law function A/N^μ shows that the error bars decrease noticeably slower than the $1/\sqrt{N}$ law. Typical values of μ are between 0.3 and 0.4.

Finally, we can compare different schemes of measurements using the 95% confidence interval as an estimate of

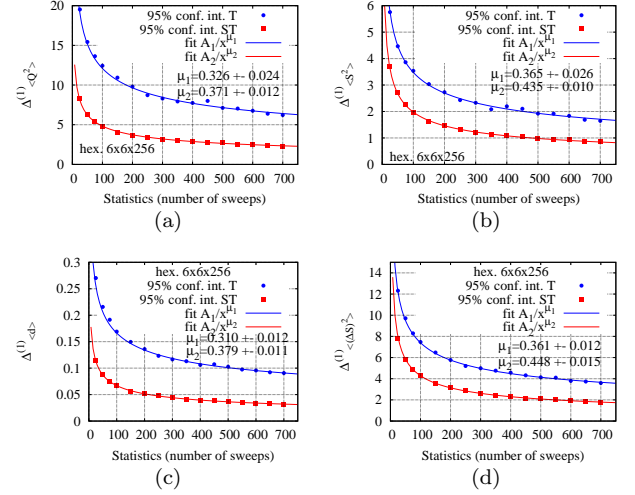


FIG. A.3. Comparison of error bars (width of the 95% confidence interval) for different observables depending on the number of sweeps N per simulation and on the employed algorithm: T-local or ST-local measurements. The top left plot shows the sublattice charge fluctuations, the top right corresponds to the sublattice spin fluctuations, bottom left is the double occupancy and bottom right the squared staggered moment. In all cases we perform power law fits. The values of the powers μ for all cases are inserted as labels in the plots. The data set was produced on the $6 \times 6 \times 256$ hexagonal lattice at $U = 5.0$ and $\beta = 20.0$. The staggered mass is set to zero.

the error bar. This comparison is done in Fig. A.3 for the $6 \times 6 \times 256$ lattice and for four different observables. In Fig. A.4 the comparison is carried out for the sublattice spin and charge fluctuations and on different lattices. We generally compare only ST-local and T-local measurements, since the global measurement scheme is not competitive. As one can see, the error bar is typically two to four times smaller for the ST-local scheme. This speedup is larger for the double occupancy and for the sublattice charge fluctuations, but smaller for observables involving spin: compare right and left columns in Fig. A.3. As apparent from the comparison of Figs. A.3(a) and A.4(a), the speedup increases with the system size.

Generically, the dependence of the error bar on the number of sweeps, N , in a given simulation can be described by the power law

$$\Delta_O^{(1)} = \frac{A}{N^\mu}, \quad (\text{A5})$$

with power μ and prefactor A dependent on the measurement scheme, the lattice size, etc. An important observation is that μ is consistently larger for ST-local measurements, thus the confidence interval decreases faster in that case and the speedup will increase with decreasing error bar. For the speedup presented in Fig. 9 in the main text, we use a conservative estimate corresponding to the largest μ within the error bars for T-local measurements and the smallest μ within the error bars for the ST-local measurements.

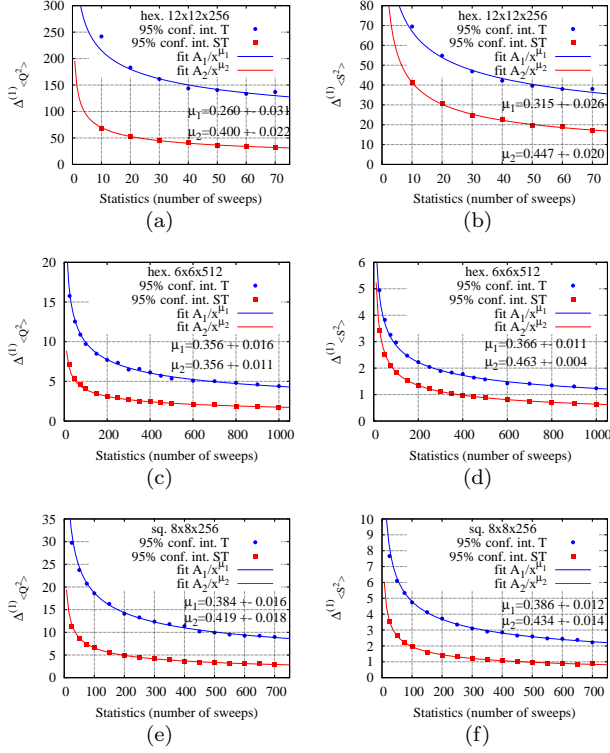


FIG. A.4. Comparison of error bars (width of the 95% confidence interval) for the sublattice charge fluctuations (left column) and sublattice spin fluctuations (right column) depending on the number of sweeps per simulation and for different models and lattices. First (upper) row corresponds to a $12 \times 12 \times 256$ hexagonal lattice, the second row shows the results for a $6 \times 6 \times 512$ hexagonal lattice and the third row corresponds to the square lattice Hubbard model on an $8 \times 8 \times 256$ lattice. Here we consider $U = 5.0$ and $\beta = 20.0$. For comparison with the $6 \times 6 \times 256$ lattice, one can refer to the upper row in Fig. A.3.

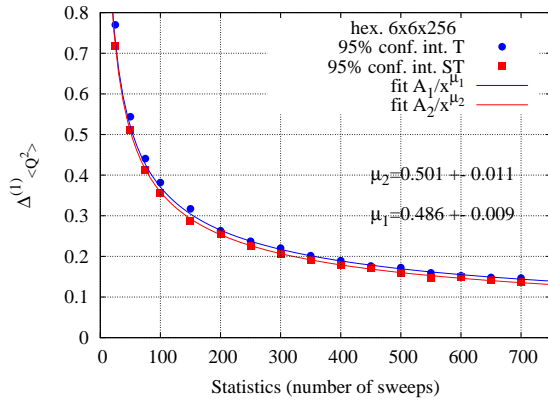


FIG. A.5. Error bars (width of the 95% confidence interval) for the sublattice charge fluctuations as a function of the number of sweeps per simulation. Calculations were done on the $6 \times 6 \times 256$ hexagonal lattice with the mass term $m = 0.1$. The mass term removes the zeros from the fermion determinant. Power law fits with their respective coefficients μ are shown in the plot. Here we consider $U = 5.0$ and $\beta = 20.0$.

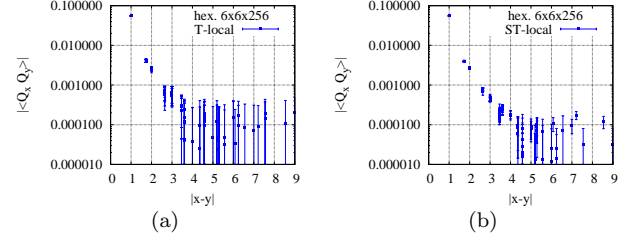


FIG. A.6. Comparison of charge-charge correlators computed with the same statistics (1000 sweeps through the lattice) using T-local measurements and ST-local measurements. The distance between sites is in units of the separation between nearest neighbours. Here we consider a $6 \times 6 \times 256$ lattice at $\beta = 20$ and $U = 5$.

Up to now, we have considered cases where the fermion determinant possesses zeros. Fig. A.5 shows the case of non-zero explicit mass term 38 inserted in the Hamiltonian 25. The differences between T-local and ST-local measurements disappear: both constant prefactor A and the power μ are identical within the quoted uncertainty.

Another characteristic example of the reduction of error bars is shown in Fig. A.6. We compare the charge-charge correlator computed within the T-local (Fig. A.6(a)) and ST-local (Fig. A.6(b)) schemes. The improvement of the error bars is noticeable. In the latter figure we can reliably trace the correlator up to the distance of 4 lattice units, while for the T-local scheme we control the correlator data up to $|x - y| = 3$.

Appendix B: Power law in distributions of observables

In this appendix we derive the power law 19 for the distribution of observables in the case of real QMC simulations for continuous auxiliary fields.

Let us consider the complementary cumulative distribution function for some four-fermion observable Θ . Among other terms, Θ always includes the second power of Euclidean fermionic propagator g^2 . This is the most important term in the vicinity of the configurations where the fermion determinant is zero, since the propagator diverges there as $1/\Delta$, where Δ is the distance to the zero point of the determinant in the space of auxiliary fields $\phi_{i,\tau}$. Due to the divergence of observables near the zero points of the determinant, exactly these field configurations define the complementary cumulative distribution function $\bar{F}_\Theta(\theta)$ at large values of the observable. The asymptotic behaviour of the function \bar{F} can be described by the integral:

$$\bar{F}_\Theta(\theta) = \mathcal{P}(\Theta > \theta) = \int_{V: \Theta > \theta} d^N \phi P(\phi), \quad (\text{B1})$$

where $P(\phi)$ is the probability distribution for the ϕ fields and N corresponds to the total number of HS fields.

First we consider the case where the zeros of determinant form “domain walls” in configuration space. If θ is sufficiently large, the volume V is just some thin layer in the vicinity of the “domain wall”, where $P(\phi) = 0$. Now we change the variables so that $x_2 \dots x_N$ correspond to the shift parallel to the “domain wall” while the coordinate x_1 is perpendicular to it. The “domain wall” itself corresponds to $x_1 = 0$. Thus

$$\bar{F}_\Theta(\theta)|_{\theta \rightarrow \infty} = \int_{V: \Theta > \theta} d^N x \frac{\mathcal{D}(\phi)}{\mathcal{D}(x)} x_1^2 f(x_2 \dots x_N), \quad (\text{B2})$$

and we used Eq. 27 in order to estimate the probability distribution $P(x)$ in the vicinity of “domain walls” as $P(x) \approx x_1^2 f(x_2 \dots x_N)$. This estimation follows from the equivalence of fermion determinants for electrons and holes at half filling. Since the observable diverges as we approach the “domain wall”:

$$\Theta \approx \frac{C(x_2, \dots x_N)}{x_1^2}, \quad (\text{B3})$$

the integral over x_1 in B2 has the limits

$$x_1 \in [-C_1(x_2, \dots x_N)/\sqrt{\theta}, C_2(x_2, \dots x_N)/\sqrt{\theta}], \quad (\text{B4})$$

where $C_1, C_2 > 0$. If the Jacobian doesn't have any divergences in the limit $x_1 \rightarrow 0$, the integral over x_1 in B2 can be computed separately. Thus the asymptotic behaviour of the function \bar{F} is described by the expression:

$$\bar{F}_\Theta(\theta)|_{\theta \rightarrow \infty} \approx \frac{\mathcal{C}}{\theta^{3/2}}, \quad (\text{B5})$$

$$\mathcal{C} = \frac{1}{3} \int dx_2 \dots dx_N \left. \frac{\mathcal{D}(\phi)}{\mathcal{D}(x)} \right|_{x_1=0} \times \quad (\text{B6})$$

$$\times (C_1(x_2, \dots x_N)^3 + C_2(x_2, \dots x_N)^3).$$

Conversion to the probability distribution gives

$$P_\Theta(\theta)|_{\theta \rightarrow \infty} \sim \frac{1}{\theta^{5/2}}. \quad (\text{B7})$$

The derivation can also be modified to accommodate the case when the dimensionality of the manifolds with zero determinant is reduced to $N - 2$, where N is the total number of auxiliary fields ϕ . We should now separate two coordinates x_1 and x_2 which corresponds to the shift perpendicular to the “line” with zero fermion determinant, while all other coordinates $x_3, \dots x_N$ again correspond to the shift parallel to this “line”. After it x_1 and x_2 are changed to polar coordinates (ρ, φ) and the resulting asymptotic behaviour for the complementary cumulative distribution function is described by the expression

$$\bar{F}_\Theta(\theta)|_{\theta \rightarrow \infty} \approx \int d\varphi dx_3 \dots dx_N \quad (\text{B8})$$

$$\int_0^{C(\varphi, x_3, \dots x_N)/\sqrt{\theta}} \rho^3 d\rho \left. \frac{\mathcal{D}(\phi)}{\mathcal{D}(x)} \right|_{\rho=0} f(\varphi, x_3 \dots x_N).$$

An additional power of ρ appears from the transfer to polar coordinates. Alternatively, one can say that this power appears from the Jacobian if the transfer to polar coordinate is included in the general change of variables $\phi \rightarrow x$. The probability distribution for the observable Θ has now the asymptote

$$P_\Theta(\theta)|_{\theta \rightarrow \infty} \sim \frac{1}{\theta^3}. \quad (\text{B9})$$

Similar derivations can be repeated for lower dimensions of the manifolds with zero fermion determinant with larger powers of ρ appearing from the Jacobian. Generally, the lower the dimensionality of the manifolds with zero fermion determinant leads to the larger absolute value of the power in the tail of the distribution.